

Igor Ostanin

Department of Civil Engineering,
University of Minnesota,
500 Pillsbury Drive SE,
Minneapolis, MN 55455
e-mail: ostan002@umn.edu

Roberto Ballarini¹

Mem. ASME
Department of Civil Engineering,
University of Minnesota,
500 Pillsbury Drive SE,
Minneapolis, MN 55455
e-mail: broberto@umn.edu

Traian Dumitrică

Mem. ASME
Department of Mechanical Engineering,
University of Minnesota,
111 Church Street SE,
Minneapolis, MN 55455
e-mail: tdraian@me.umn.edu

Distinct Element Method Modeling of Carbon Nanotube Bundles With Intertube Sliding and Dissipation

The recently developed distinct element method for mesoscale modeling of carbon nanotubes is extended to account for energy dissipation and then applied to characterize the constitutive behavior of crystalline carbon nanotube bundles subjected to simple tension and to simple shear loadings. It is shown that if these structures are sufficiently long and thick, then they become representative volume elements. The predicted initial stiffness and strength of the representative volumes are in agreement with reported experimental data. The simulations demonstrate that energy dissipation plays a central role in the mechanical response and deformation kinematics of carbon nanotube bundles. [DOI: 10.1115/1.4026484]

1 Introduction

Carbon nanotube (CNT) based materials, and in particular CNT bundles and CNT ropes, show great promise for technological applications [1–13]. Twisted CNT yarns are candidate structures for electromechanical torsional actuators and artificial muscles [10]. Crystalline CNT bundles and CNT ropes, consisting of micrometer-long CNTs, are of great interest as wires and cables with high tensile load bearing capacity [7–9,13] and thin and flexible conductors that can be embedded onto polymer composites [12].

Predicting the mechanical response of CNT-based materials from the properties of and interactions between individual nanotubes has been a challenging mechanics problem. While molecular dynamics (MD) has been applied successfully to model the mechanical and physical properties of single CNTs [14–17], computational limitations related to affordable simulation times and system sizes do not allow applying MD to problems of collective mechanical behavior of large assemblies of CNTs. These limitations have led to the development of numerous empirical and theoretical mesoscopic models for studying the behavior of CNT structures [18–28] including our distinct element method (DEM) for CNTs [29,30]. Starting from the atomic-level description, these models rely on coarse-graining procedures to reduce the number of degrees of freedom (DOF) in order to make simulations manageable.

In DEM, we represent a CNT by a chain of distinct elements interacting with each other via prescribed contact models informed by accurate simulations at the atomistic scale. These contact models capture both the covalent intratube binding and the van der Waals (vdW) intertube microscopic forces. We demonstrated the suitability of the DEM methodology to investigate the mechanics of large-scale CNT systems, including nanotube ropes, rings, and films.

Using the DEM methodology, in this paper we consider two aspects of the mechanics of CNT bundle that have not yet been

adequately addressed in the literature. The first is the question of whether a bundle composed of CNTs interacting via vdW forces can be considered a representative volume element (RVE). Considering that CNT-based structures are candidates for technological applications involving mechanical forces, it is remarkable that this question has not yet been answered. The second is the role of intrinsic energy dissipation, which involves energy transfer from the coherent mechanical motion into the internal energy (stochastic motion) of the carbon atoms. Experiments [4,31,32] suggest that energy dissipation is an essential feature of the mechanical response of pure CNT materials and CNT composites. Therefore, it should be included in mesoscopic models of CNT structures. Investigating these two aspects becomes meaningful in the context of our recent work [30] on developing a vdW contact model that produces a smooth intertube potential energy surface for CNTs sliding against each other. This model is in agreement with the microscopic level picture, where there is convincing evidence that the corrugation potential associated with the vdW registry is small [33].

In this paper, we show that the two aspects of representative mechanics for the volatile CNT bundle system and the energy dissipation are strongly connected. The paper is organized as follows. Section 2 summarizes the DEM methodology applied for (10,10) CNTs, that were parameterized [30], and delineates the treatment of energy dissipation. In Sec. 3, the mesoscopic model is used to simulate the response to simple tension and simple shear loadings of crystalline CNT bundles. The results demonstrate that in the presence of sufficient energy dissipation, large enough crystals behave as RVEs (the stress-strain curves of specimens that are larger than the RVE are weak functions of their size). In Sec. 4, we make connections with existing experiments and give our conclusions.

2 Simulation Method and Procedure

The first application of the DEM to the problem of mesoscopic modeling of CNT systems was presented in Ref. [30]. This approach is based on a coarse-graining of the atomistic structure of a CNT into a system of interacting rigid particles. The interactions between these particles are derived from the results of finer-scale MD simulations. Here, we review the DEM model and describe its new features.

¹Corresponding author.

Contributed by the Applied Mechanics Division of ASME for publication in the JOURNAL OF APPLIED MECHANICS. Manuscript received November 27, 2013; final manuscript received January 9, 2014; accepted manuscript posted February 3, 2014; published online February 3, 2014. Editor: Yonggang Huang.

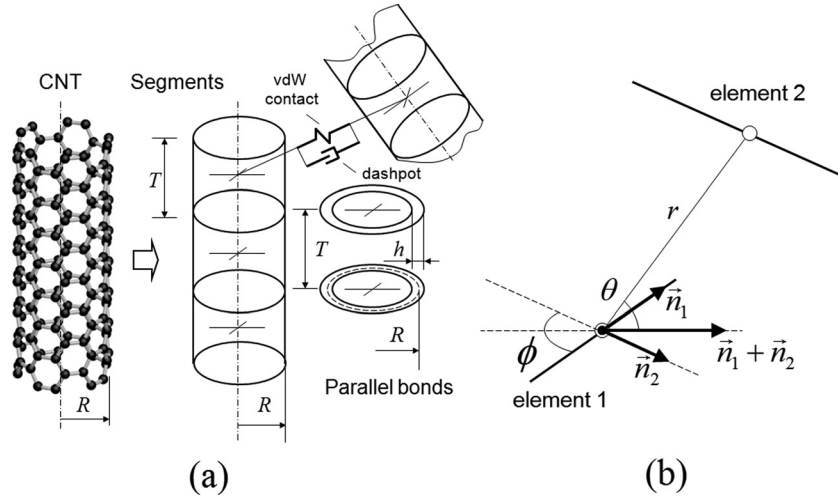


Fig. 1 (a) Coarse graining of a CNT into a chain of cylindrical segments, representing inertial properties of a CNT. Segments are linked with parallel bond interfaces, representing elastic properties of a CNT surface, arising from covalent bonds between C atoms within the CNT surface. Segments of neighboring CNTs interact via mesoscopic vdW contact model, acting in parallel with viscous forces that damp relative translational motion of CNT segments. (b) Illustration of definition of generalized coordinates r , θ , ϕ for two interacting cylindrical segments of neighboring CNTs. \vec{n}_1 and \vec{n}_2 are axial directions of first and second cylinder.

2.1 Damped Dynamic of CNT Elements. Within DEM, a CNT is represented by a chain of rigid hollow cylindrical segments, which are the distinct elements. Each segment has a unit aspect ratio, i.e., its length T is twice the radius of a CNT R (Fig. 1(a)). For (10,10) CNTs, such segment lumps approximately 220 carbon atoms. Each segment is characterized by mass m and inertia tensor I_{ij} . Cartesian components of inertia tensor of a hollow cylindrical segment with an axis parallel to z coordinate axis are

$$I_{11} = I_{22} = \frac{m}{12}(6R^2 + T^2), \quad I_{33} = mR^2, \quad I_{ij}^{(i \neq j)} = 0 \quad (1)$$

The values of mass m and components (Eq. (1)) for (10,10) CNTs are given in Table 1. Translational motions of cylindrical segments are calculated with conventional velocity Verlet time integration scheme. Rotational motions are integrated with fourth order Runge–Kutta method, combined with a quaternion representation of rotations [34].

The coarse-graining (homogenization) leads to the complete elimination of atomistic DOFs. Therefore, the dissipative microscopic processes associated with CNT sliding are not explicitly captured and should be included in a phenomenological manner. In this respect, our model presents two channels of energy dissipation—local damping and viscous damping, characterized by parameters α and β , respectively [35].

Local damping is introduced with the sole goal of stabilizing the nonsymplectic time integration. It acts on each element and applies components of damping force F_i^z (moment M_i^z) proportional to the corresponding components of unbalanced force F_i (moment M_i) according to

$$F_i^z = -\alpha F_i \text{sign}(v_i), \quad M_i^z = -\alpha M_i \text{sign}(\omega_i), \quad i = 1 \dots 3 \quad (2)$$

Here v_i and ω_i are components of the translational and rotational velocity of an element, and $\text{sign}(x)$ is the sign function.

We utilize viscous damping, to capture the complex energy losses during CNT sliding. Micromechanisms of such losses were described qualitatively in Ref. [31]. They are associated with forced vibrations of carbon atoms that are pulled out of their vdW registry.

Experimental works [4,33] reveal rate dependence of such losses. Therefore, the effective dissipative force acting between two CNT surfaces can be modeled as a dashpot (Fig. 1(a)), acting in parallel with the vdW contact model. Normal F_n^β and tangential F_s^β forces developed by the dashpot are proportional to normal v_n and tangential v_s relative velocities of elements in vdW contact

$$F_n^\beta = c_n v_n, \quad F_s^\beta = c_s v_s \quad (3)$$

Viscosity coefficients c_n and c_t are related to β as follows:

$$c_n = 2\beta\sqrt{Mk_n}, \quad c_t = 2\beta\sqrt{Mk_t} \quad (4)$$

where k_n and k_s are stiffnesses of the contact model, here taken $k_n = 100 \text{ eV/nm}^2$, $k_s = 100 \text{ eV/nm}^2$.

Coefficient β has the meaning of damping ratio.

Unfortunately, a direct, microscopic calibration of damping has proven to be insurmountable to date. Therefore, a top-down approach is used here, where the viscous damping coefficient is a free parameter chosen to reproduce the mechanical behavior observed experimentally. Thus, rather than predicting quantitatively-correct rate-dependent mechanical properties, the goal of our effective damping approach is to reveal the role of energy dissipation processes on the mechanics of CNT materials. The simulations presented in this paper were performed with the fixed time step of 10 fs. Maximum local damping value $\alpha = 0.7$ is used to ensure the time integration stability [34]. The value of viscous damping $\beta = 0.03$ is chosen in a top-down way to reproduce the realistic energy balance in a mechanical simulation (see Sec. 4).

2.2 Parallel Bond Contact Model. Neighboring distinct elements representing a CNT are interacting with elastic parallel bonds that capture the linear elasticity of CNT walls [30]. A parallel bond provides an interface of distributed springs that resist stretching, shearing, bending, and torsional deformations, according to the following incremental laws:

$$\begin{aligned} \Delta x &= -k_n^b \bar{A} \Delta F_n, & \Delta y &= -k_s^b \bar{A} \Delta F_s, & \Delta \theta &= -k_n^b \bar{I} \Delta M_n, \\ \Delta \phi &= -k_s^b \bar{J} \Delta M_s \end{aligned} \quad (5)$$

Table 1 Parameters of DEM model for (10,10) CNTs

		Geometry, mass, and moment of inertia of a segment				
R , nm	T , nm	m , amu	I_{11} , amu \times nm ²	I_{22} , amu \times nm ²	I_{33} , amu \times nm ²	
0.678	1.356	2649	1014.75	1014.75	1217.7	
Parameters of parallel bond contact model						
k_n , eV / nm ⁴	k_s , eV / nm ⁴	\bar{A} , nm ²	\bar{I} , nm ⁴	\bar{J} , nm ⁴		
4740	2110	1.427	0.348	0.696		
Parameters of vdW contact model						
ϵ' , meV	α'	β'	A'	B'	δ'	C_ϕ
149.3	9.5	4	0.0223	1.31	-7.5	90
k	C_1	C_2	C_3	C_4	C_5	
5	0.35819	0.03263	-0.00138	-0.00017	0.00024	
Q_1	Q_2	Q_3	Q_4	Q_5		
-80.0	288.0	-336.0	128.0			

where \bar{A} , \bar{I} , and \bar{J} are area, moment of inertia, and polar moment of inertia of a cylindrical cross section,

$$\bar{A} = 2\pi Rt, \quad \bar{I} = \pi R t (R^2 + 0.25t^2), \quad \bar{J} = 2\bar{I} \quad (6)$$

$k_n^b = E_{\text{CNT}}/T$, $k_s^b = G_{\text{CNT}}/T$ are the distributed normal and shear stiffnesses of a CNT bond contact; $t = 0.335$ nm is the thickness of the CNT wall, accepted to be equal to interlayer vdW spacing; $E_{\text{CNT}} = 1029$ GPa, $G_{\text{CNT}} = 459$ GPa are values of CNTs Young's and shear moduli, respectively, which are determined from the results of atomic-scale simulations [15]. Variables $\Delta x, \Delta y, \Delta\theta, \Delta\phi$ denote increments of normal and shear displacement components, and bending and twisting angles; $\Delta F_n, \Delta F_s, \Delta M_n, \Delta M_s$ are increments of normal force, shear force, bending moment, and twisting moment. A chain of parallel bonded elements behaves as an elastic beam with corresponding cross section and elastic moduli.

2.3 vdW Contact Model. The elements of neighboring CNTs interact via a vdW contact model. Accurate derivation and detailed description of the potential is presented in Refs. [29,30]. Unlike simple isotropic pair potentials, which are typically used in particle-based approaches, our contact model reproduces near-field anisotropy of interacting cylindrical segments, which leads to realistic representation of adhesive interactions of CNTs. In particular, the realistic vdW contact model resolves relative sliding of CNTs in contact. An anisotropic potential has the following shape:

$$\begin{aligned}
 U(r, \theta, \phi) &= f_c(r) V^k(r, \theta) \Phi(r, \phi) \\
 V^k(r, \theta) &= \epsilon' \left(\frac{A'}{D^k(r, \theta)^{\alpha'}} - \frac{B'}{D^k(r, \theta)^{\beta'}} \right) \\
 D^k(r, \theta) &= \frac{r}{R \Theta^k(\theta)} - 2 \\
 \Phi(r, \phi) &= 1 + W_\phi(r) (1 - \cos(2\phi)) \\
 \Theta^k(\theta) &= 1 + \sum_{i=1}^k C_i ((-1)^{i-1} + \cos(2i\theta)) \\
 W_\phi(r) &= C_\phi (r/R)^{\delta'} \\
 f_c(r) &= \sum_{i=0}^3 Q_i (r/8R)^i \quad (7)
 \end{aligned}$$

Potential U depends on three variables—the distance between segments r and angular variables θ and ϕ , defined according to Fig. 1(b). The potential is designed as a generalized Lennard–Jones pair potential V , modified with angular adjustments Θ and Φ , in order to provide translational symmetry of the potential of two infinite parallel CNTs and aligning moments acting between misaligned segments [30]. Full parameterization of the potential is

presented in Table 1. The normal and shear contact force, as well as the contact moment are defined as

$$F_r = -\frac{\partial U}{\partial r}, \quad F_\theta = -\frac{1}{r} \frac{\partial U}{\partial \theta}, \quad M_\phi = -\frac{\partial U}{\partial \phi} \quad (8)$$

2.4 Mechanical Test With DEM Model. We now present the procedure for the self-assembly and loading of a CNT bundle model that is used in the tension DEM tests described in Sec. 3. Figure 2(a) presents a schematic of a close-packed bundle of CNTs with a hexagonal cross section. The side of a hexagon is $(N - 1)r_0$, where N is the number of tubes along the side and $r_0 = 1.71$ nm is the equilibrium center-to-center distance between the constituent (10,10) CNTs. The number of CNTs that define the bundle cross section and its effective area write

$$\begin{aligned}
 N_{\text{CNT}} &= 1 + 3N(N - 1) \\
 S &= \frac{3\sqrt{3}}{4} [1 + 3N(N - 1)] r_0^2 \quad (9)
 \end{aligned}$$

The bundle of length L is composed of individual CNTs with length L_{CNT} , where $L_{\text{CNT}} < L$. The ratio $M = L/L_{\text{CNT}}$ will be referred to as *length factor* of a CNT bundle. In a row of CNTs (along the x direction), there is no spacing between the CNT caps (Fig. 2(a)); vdW interaction between the caps is not prescribed. For each row, the positions of CNT joints is defined by the distance L_i between one of the edges of a bundle and the nearest CNT edge (Fig. 2(a)); L_i is random with uniform distribution on the interval $(0, L_{\text{CNT}})$.

A bundle specimen is assembled in the following way: A hexagonal CNT bundle, described above, is generated at time zero and allowed to relax for 10,000 cycles, or 0.1 ns (it is worth noting here that the time of this evolution is affected by the damping present in the mesoscale model and does not directly correspond to the time of evolution in the full atomistic model). We observe that the bundle contracts in the x -direction (Fig. 2(b)), leading to approximately 0.3% decrease in length and an elastic strain energy of approximately 0.5 kJ/kg (Fig. 2(c)). In this stage of initial relaxation, bundles may also develop lateral deformations and store part of elastic energy in bending. This behavior is due to inherent asymmetry of random positions of joints. As one can see from Fig. 2(c), initial relaxation does not bring the bundle to a global equilibrium. However, the relaxation time is sufficient to exclude the influence of relaxation processes on the stress response during the test.

After the relaxation is completed, two layers of distinct elements at both edges of a bundle are designated as grips. The elements between grips represent the gage of length $L_g = L - 2T$ (Fig. 2(d)). The x degree of freedom of grip elements are fixed, and the bundle is equilibrated for an additional 1000 cycles (0.01 ns) in order to ensure that the initial force acting on each grip is zero. A displacement controlled loading is achieved next

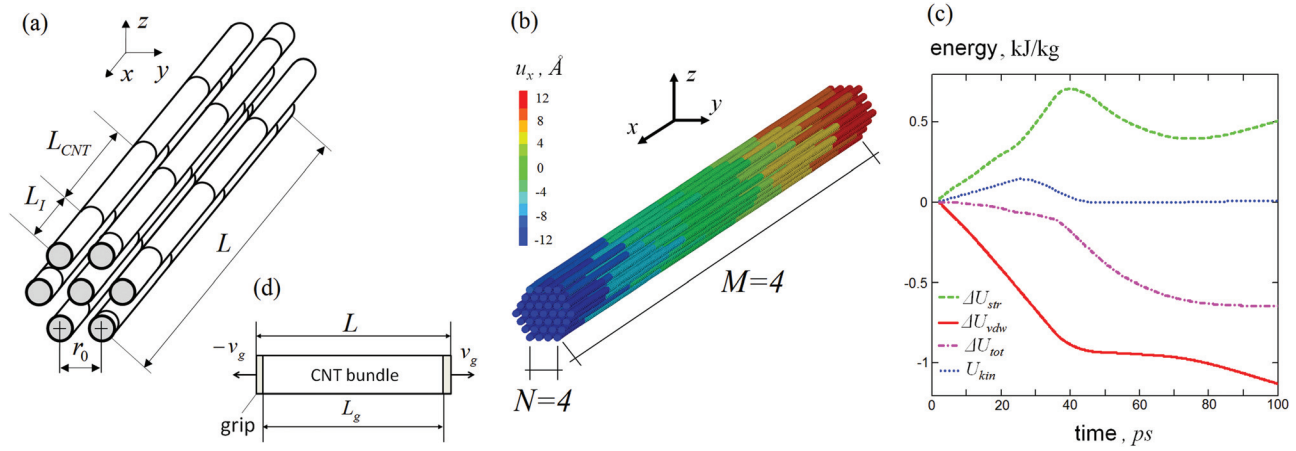


Fig. 2 (a) Schematics of a crystalline CNT bundle ($N = 2$). (b) Geometry of the prerelaxed bundle ($N = 4$, $M = 4$). Color legend gives x -component of displacements developing during the relaxation. (c) Changes in different terms of CNT bundle energy during prerelaxation. The change in strain energy ΔU_{str} , vdW adhesion energy ΔU_{vdw} , total energy ΔU_{tot} , and kinetic energy U_{kin} are presented. (d) Gage and grip regions of a CNT bundle specimen.

Table 2 Parameters of the tested specimens of CNT bundles

Specimen	$L, \mu\text{m}$	M	$L_{CNT}, \mu\text{m}$	N	N_{CNT}	$v_g, \text{m/s}$
1	0.133	2	0.068	4	37	1.33
2	0.2	3				2
3	0.267	4				2.67
4	0.333	5				3.33
5	0.4	6				4
6	0.467	7				4.67
7	0.533	8				5.33
8	0.6	9				6
9	0.667	10				6.67
10	0.267	2	0.136	4	37	2.67
11	0.4	3				4
12	0.533	4				5.33
13	0.667	5				6.67
14	0.8	6				8
15	0.933	7				9.33
16	1.067	8				10.67
17	1.2	9				12
18	1.333	10				13.33
19	0.267	4	0.068	2	7	2.67
20				3	19	
21				4	37	
22				5	61	
23				6	91	
24				7	121	
25	0.533	4	0.136	2	7	5.33
26				3	19	
27				4	37	
28				5	61	
29				6	91	
30				7	121	

by prescribing that both grips accelerate from 0 to the given velocity v_g ($-v_g$) during 5000 cycles (0.05 ns). This acceleration period is used to reduce the dynamic response, which is significant in case of instantaneous acceleration of the grips.

3 Results

3.1 Size Convergence Studies of Stress-Strain Curves in Tensile Tests. We investigate the behavior of CNT bundles subjected to simple tension loading aiming to establish if an RVE can be achieved. Systematic tensile tests have been carried out for a collection of CNT bundles with different values of the L , L_{CNT} , N ,

and M bundle parameters, as given in Table 2. Stress-strain curves (SSCs) were plotted during each test, see Figs. 3(a) and 3(b) and Figs. 3(d) and 3(e). The tensile stress is defined as $\sigma_{xx} = F_x/S$, where F_x is the x -component of force acting on the grip. The nominal strain is defined as $\epsilon_{xx} = 2u_x^g/L$, where u_x^g is the x -component of the grip displacement. Indexes of stress and strain (strain rate) are omitted below. In the described series of simulations, the bundles were elongated up to 2% strain at the strain rate $\dot{\epsilon} = 2 \times 10^7 \text{ s}^{-1}$.

A typical SSC of a CNT bundle consists of a monotonic growth region up to a peak value and a postpeak evolution. The peak value of stress, which represents the uniaxial tensile strength of a bundle (σ_{uts}), is about 1 GPa. As it can be seen in Figs. 3(c) and 3(f), it depends on M and N only for short and thin specimens, but it is size-independent for those that are representatively long and thick. Other important parameters of the SSCs—the Young's modulus of a bundle E , the critical strain ϵ_c (Table 3) at σ_{uts} , and the monotonic growth shape of the SCC curve all exhibit the same trends. Interestingly, comparison of the convergence of tensile strength for the two different values of L_{CNT} , Figs. 3(c) and 3(f), suggest that the size of an RVE has a weak dependence on L_{CNT} .

We conclude that in the monotonic growth region, the size dependences of SSCs becomes negligible for specimens with $M \geq 4$ and $N \geq 4$. Such specimens can be considered as RVEs of a CNT bundle. One can also estimate the Young's modulus of hexagonal arrangement of noninteracting individually stretched CNTs as

$$E_0 = E_{CNT} \frac{S_T}{S_C}, \quad S_T = 2\pi tr_{CNT}, \quad S_C = \frac{3\sqrt{3}}{4} r_0^2 \quad (10)$$

Based on the values for (10,10) CNTs given above, one obtains $E_0 = 385 \text{ GPa}$. As it can be seen in Table 3, the initial Young's modulus of a bundle is overall significantly smaller than E_0 . This indicates that the sliding of CNTs within a bundle significantly decreases the effective elastic modulus.

3.2 Small Deformation of a CNT Bundle: Energy Balance and Kinematics. The mechanical response of a CNT bundle presented in Sec. 3.1 is by the result of the interplay among forces of potential, inertial, and dissipative nature. In order to identify the role of each, we track during simulations the different terms of potential energy, kinetic energy, and dissipated energy. The energy balance during the displacement control tension test is given by

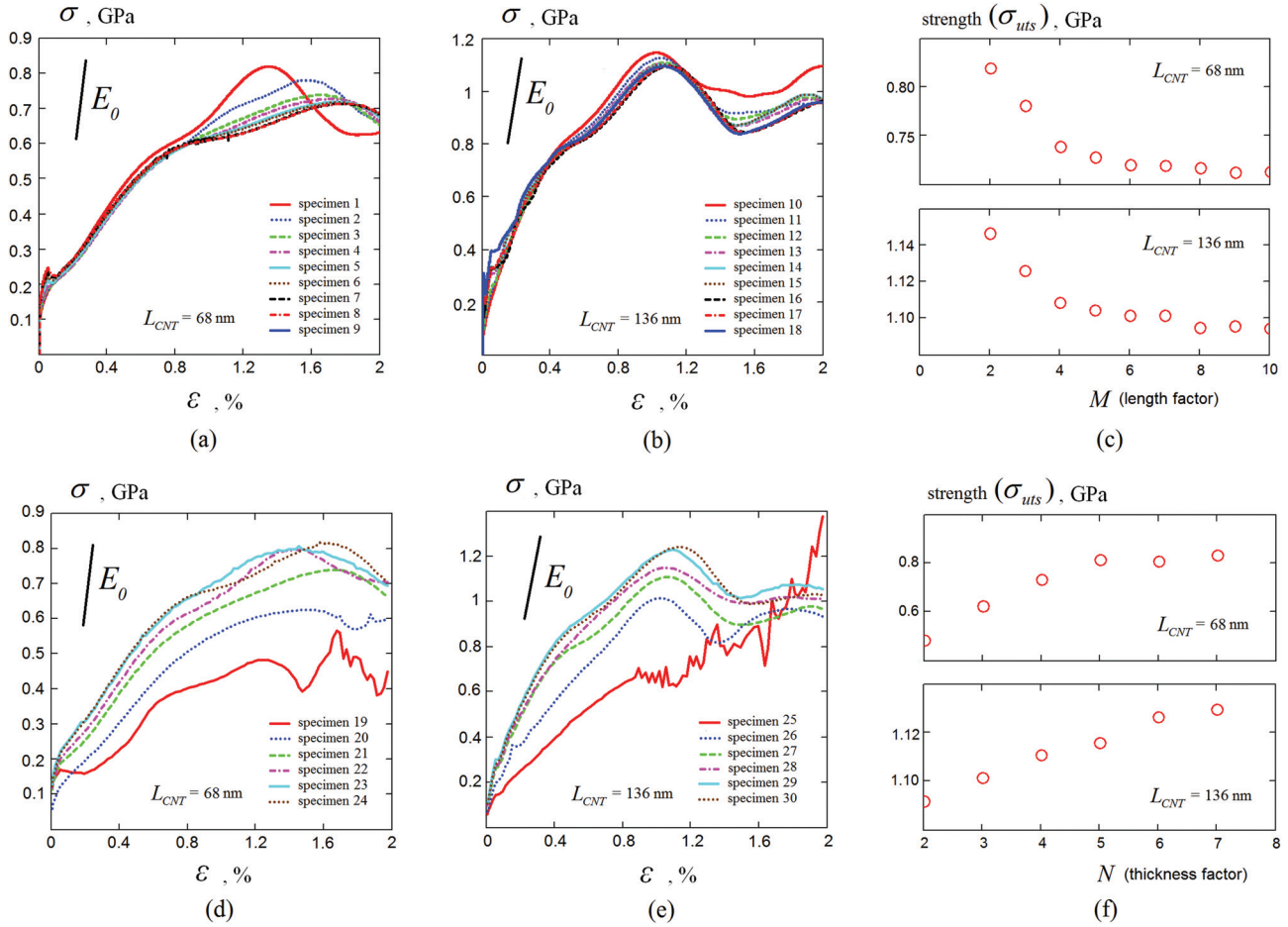


Fig. 3 (a), (b) SSCs of bundles of different length, containing 37 tubes on a cross section ($N = 4$), for $L_{CNT} = 0.068 \mu\text{m}$ (specimens 1–9, (a)) and $L_{CNT} = 0.136 \mu\text{m}$ (specimens 10–18, (b)). (c) Uniaxial tensile strength of a bundle σ_{uts} as a function of the length factor M for $L_{CNT} = 0.068 \mu\text{m}$ and $L_{CNT} = 0.136 \mu\text{m}$. (d), (e) SSCs of bundles of different thickness, with length factor $M = 4$, and $L_{CNT} = 0.068 \mu\text{m}$ (specimens 19–24, (d)) and $L_{CNT} = 0.136 \mu\text{m}$ (specimens 25–30, (e)). (f) Uniaxial tensile strength of a bundle σ_{uts} as a function of the thickness factor N for $L_{CNT} = 0.068 \mu\text{m}$ and $L_{CNT} = 0.136 \mu\text{m}$. The slope of reference lines given in figures (a), (b), (d), (e) corresponds to Young's modulus E_0 estimated for hexagonal arrangement of stretched noninteracting CNTs.

$$A_{\text{ext}}(\Delta) = \int_0^{\Delta} F_{\text{ext}}(\Delta') d\Delta' \\ = \Delta K(\Delta) + \Delta U_{\text{str}}(\Delta) + \Delta U_{\text{vdw}}(\Delta) + \Delta Q(\Delta) \quad (11)$$

Here Δ (Δ') is the absolute elongation of a CNT bundle; $A_{\text{ext}}(\Delta)$ is the work done by external force $F_{\text{ext}}(\Delta)$ during the test; $\Delta K(\Delta)$ is the change in kinetic energy during the simulation; $\Delta U_{\text{str}}(\Delta)$ is the change in total strain energy (sum of CNTs stretching, bending, shearing, and torsion); $\Delta U_{\text{vdw}}(\Delta)$ is the change in vdW adhesion energy, associated with the formation of a new vdW surface; and $\Delta Q(\Delta)$ is the energy dissipated by local and viscous damping that represents heating of a CNT bundle. In a quasi-static test, the changes in the kinetic energy appear to be negligible compared to other terms. By formal differentiation of Eq. (11) with respect to Δ and omitting the kinetic energy term, one has

$$F_{\text{ext}}(\Delta) = \frac{d(\Delta U_{\text{str}}(\Delta))}{d\Delta} + \frac{d(\Delta U_{\text{vdw}}(\Delta))}{d\Delta} + \frac{d(\Delta Q(\Delta))}{d\Delta} \quad (12)$$

Therefore, for the SSC of an RVE, one can write

$$\sigma_{\text{tot}}(\varepsilon) = \sigma_{\text{str}}(\varepsilon) + \sigma_{\text{vdw}}(\varepsilon) + \sigma_{\text{dis}}(\varepsilon) \quad (13)$$

Thus, total stress response $\sigma_{\text{tot}}(\varepsilon)$ in the quasi-static test (neglecting inertial effects) can be formally decomposed into three terms associated with elastic deformation of CNTs ($\sigma_{\text{str}}(\varepsilon)$), formation of a new vdW surface ($\sigma_{\text{vdw}}(\varepsilon)$), and dissipation ($\sigma_{\text{dis}}(\varepsilon)$). It is important to note that neither of these terms is rate- and path-independent; the presence of rate-dependent dissipation affects the whole mechanism of the deformation, i.e., the balance between stretching and sliding of CNTs.

Figures 4(a) and 4(b) presents the decomposition (11,13) for SSC of an RVE (specimen 12 in Table 2). Figure 4(a) gives the variations in different energy terms that appear in Eq. (11), and Fig. 4(b) presents the decomposition (Eq. (13)).

Initial rapid changes of the decomposition terms given in Fig. 4(b) are likely associated with dynamic effects. Omitting this initial part, we can distinguish three regions of the SSC. The first region corresponds to strains between 0.05% and 0.3% and is dominated by the elastic response of individual stretched tubes. An interesting feature is that initial elastic response is negative because, as was noticed in Sec. 2.4, CNTs in a bundle are slightly compressed by vdW adhesion forces, and at the initial stage of the test they are unstrained by external tensile load. We note that almost all strain energy in our small strain simulations is associated with the tension/compression term in Eq. (5), with less than 10% associated with bending, shear, and twisting terms.

The second part of the response (strains between 0.3% and 1%) is characterized by the changes in all energy terms; this signifies

Table 3 Results of tensile tests on CNT bundles

Specimen	E , GPa	σ_{uts} , GPa	ϵ_c , %	Specimen	E , GPa	σ_{uts} , GPa	ϵ_c , %
1	70.191	0.819	1.346	10	145.774	1.146	1.02
2	63.267	0.781	1.568	11	137.162	1.126	1.05
3	61.8	0.738	1.646	12	135.377	1.108	1.062
4	60.776	0.728	1.712	13	127.923	1.104	1.057
5	60.339	0.72	1.748	14	121.273	1.102	1.069
6	61.53	0.719	1.745	15	123.234	1.101	1.061
7	62.409	0.717	1.763	16	127.971	1.095	1.097
8	62.925	0.712	1.785	17	131.678	1.096	1.09
9	62.472	0.713	1.778	18	131.613	1.094	1.092
19	25.421	0.482	1.242	25	67.898	0.917	1.349
20	48.716	0.625	1.527	26	87.632	1.014	1.014
21	61.8	0.733	1.55	27	135.377	1.108	1.062
22	65.374	0.815	1.475	28	128.223	1.158	1.06
23	68.849	0.809	1.451	29	148.965	1.263	1.091
24	73.411	0.832	1.55	30	152.298	1.294	1.13

sliding of tubes within a bundle, accompanied by formation of new vdW surface and energy dissipation. Energy dissipation occurs without releasing the elastic strain energy accumulated in individual CNTs. These two processes dominate the prepeak shape of the SSC. The postpeak region (strains more than 1%) is characterized by the release of the elastic strain energy of the CNTs.

To visualize sliding of CNTs in a bundle, we adopt the notion of a slip vector [36], defined as

$$\vec{\delta} = -\frac{1}{\lambda_i} \sum_j^{\lambda_i} (x^{(ij)} - X^{(ij)}) \quad (14)$$

where $x^{(ij)}$ and $X^{(ij)}$ are the vector differences between the coordinates of elements i and j in the current and reference states, respectively, and λ_i is the number of nearest neighbors to element i in the initial reference configuration.

In the case of small deformation, the slip direction is always parallel to the axis of a CNT bundle. We are interested mostly in the slip vector magnitude, which is displayed in Fig. 4(c) at three representative strain levels for specimen 12 in Table 2. One can see the development of localization of the CNT sliding region. At the stage of initiation, the CNTs slipping interfaces are distributed nearly evenly along the bundle, showing, however, an initiation of periodic structure reflecting periodicity of the structure of a bundle. When approaching peak stress, deformation starts localizing, and this localization develops further in a postpeak regime. The development of localization is indicated by the magnitude of a slip vector that grows faster than the nominal strain.

3.3 Role of Dissipation. The mechanical behavior of CNT bundles depends on the rate of energy dissipation. Figure 5(a) gives SSCs, obtained in a tensile test identical to size convergence tests described above but without viscous damping ($\beta = 0$) and with a relatively small value of local damping. Stress-strain curves obtained in such a test demonstrate size dependence. Analysis of CNT kinematics (Fig. 5(b)) indicates that specimens immediately develop localized failure. Figure 5(c) demonstrates the effect of local and viscous damping on deformation localization. The figure shows the distribution of slip vector magnitude, averaged over thin slices along the length of a specimen. The localization is controlled mostly by viscous damping. On one hand, if $\beta = 0$ slip is immediately localized close to the grips. On the other hand, $\beta = 0.03$ leads to a nearly uniform distribution of slip along the

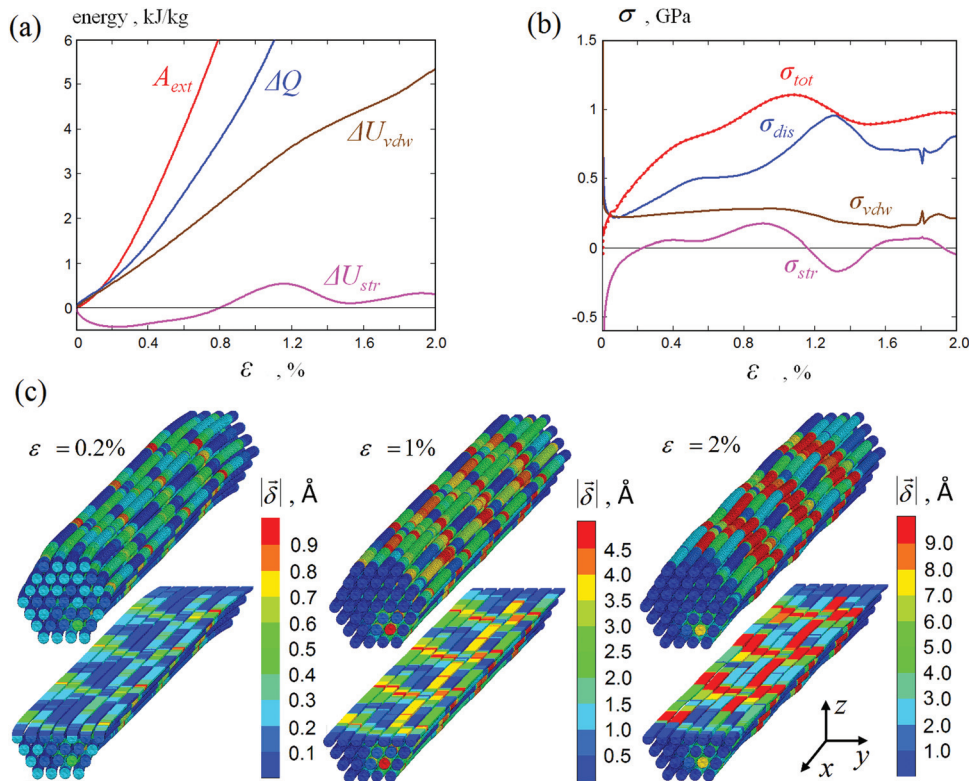


Fig. 4 (a) Work of external force A_{ext} , as compared to changes in elastic strain energy ΔU_{str} , vdW adhesion energy ΔU_{vdw} , and dissipated energy ΔQ during the test. **(b)** Terms of decomposition (Eq. (13)) during the simulation. Total stress response σ_{tot} is calculated as a sum of derivatives of traced energy terms (dashed line) and directly from force balance (solid line). **(c)** Development of a localized deformation in a CNT bundle. Visualization of CNT bundle geometry and magnitude of a slip vector (on the surface of a bundle and on a horizontal axial cross section of a bundle).

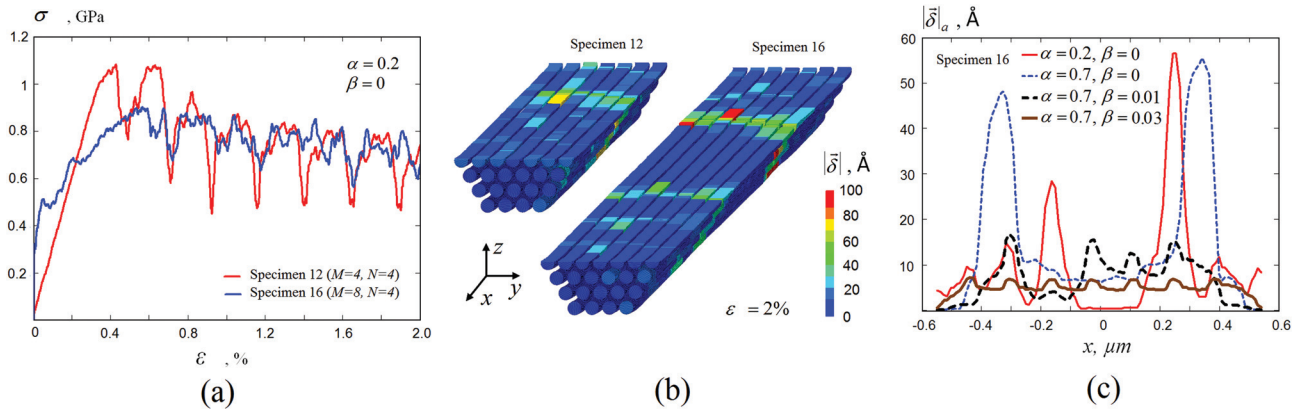


Fig. 5 Low damping ($\alpha = 0.2$, $\beta = 0.0$) mechanical tests on CNT bundles. (a) Stress-strain curves for specimen 12 and specimen 16 in Table 2 indicate the absence of an RVE. (b) Magnitude of slip vector, visualized on a horizontal axial cross-section, indicates immediate localization of the deformation and brittle fracture of a specimen. (c) Magnitude of a slip vector, averaged over thin slices of a bundle (specimen 16) along the length for few different values of viscous and local damping.

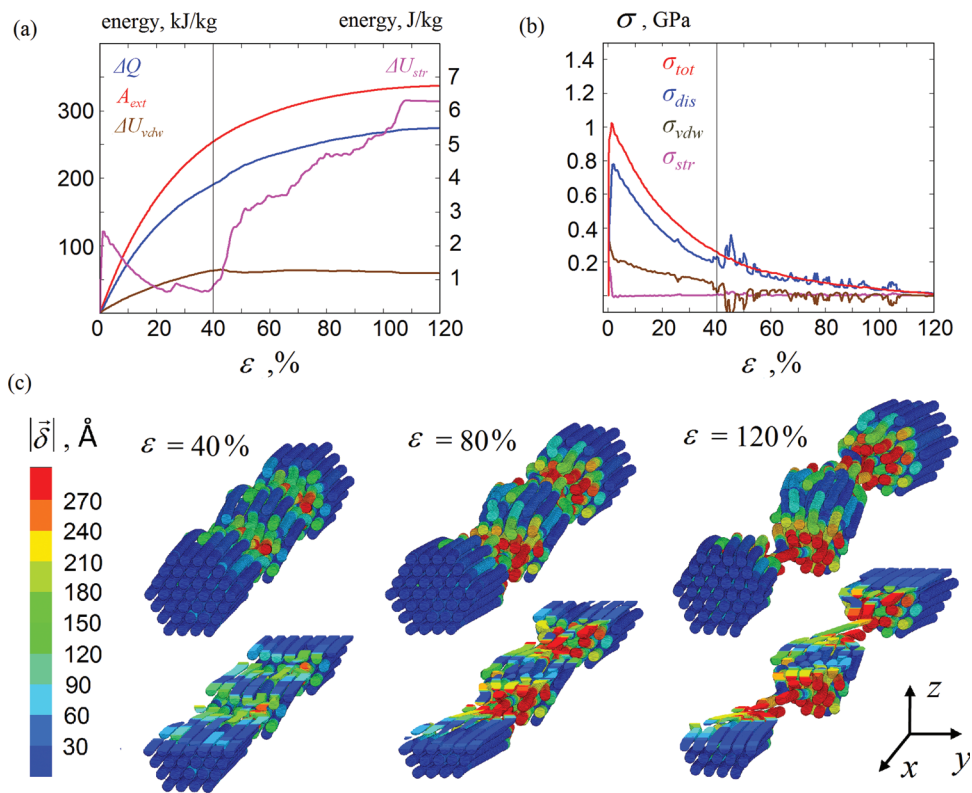


Fig. 6 Large deformation of a CNT bundle. (a) Work of external force A_{ext} , as compared to changes in elastic strain energy ΔU_{str} , vdW adhesion energy ΔU_{vdw} , and dissipated energy ΔQ during the test. (b) Terms of decomposition (Eq. (13)) during the simulation. (c) CNT bundle geometry and magnitude of a slip vector on the surface of a bundle and on a horizontal axial cross section of a bundle.

length and size-independent (material) response. As far as the localization phenomena is controlled by the magnitude of viscous forces between CNTs, it equivalently depends on damping ratio and strain rate.

3.4 Large Strain Deformation and Failure. So far we have been considering small deformation of CNT bundles under tensile load. In this section, we give a qualitative picture of a large strain deformation and breakage of a representatively large CNT bundle. Consider specimen 2 from Table 2, subjected to a large strain test. Strain is applied at a fixed rate of $\dot{\epsilon} = 2 \times 10^8 \text{ s}^{-1}$ in a

displacement control mode until the specimen's breakage. The initial regime of postpeak deformation is characterized by smooth sliding of CNTs along each other with slip direction parallel to an axis of the bundle. This regime of the deformation is characterized by nearly linear changes in vdW adhesion energy, and a gradual decrease in elastic energy (Fig. 6(a)). The strain softening behavior (Fig. 6(b)) is conditioned by a decrease of the averaged length and number of vdW contacts between CNTs, and corresponding decrease in viscous and potential forces, acting between CNT interfaces.

At the initial stage of postpeak deformation, one can see the development of CNT sliding in periodically located slip zones

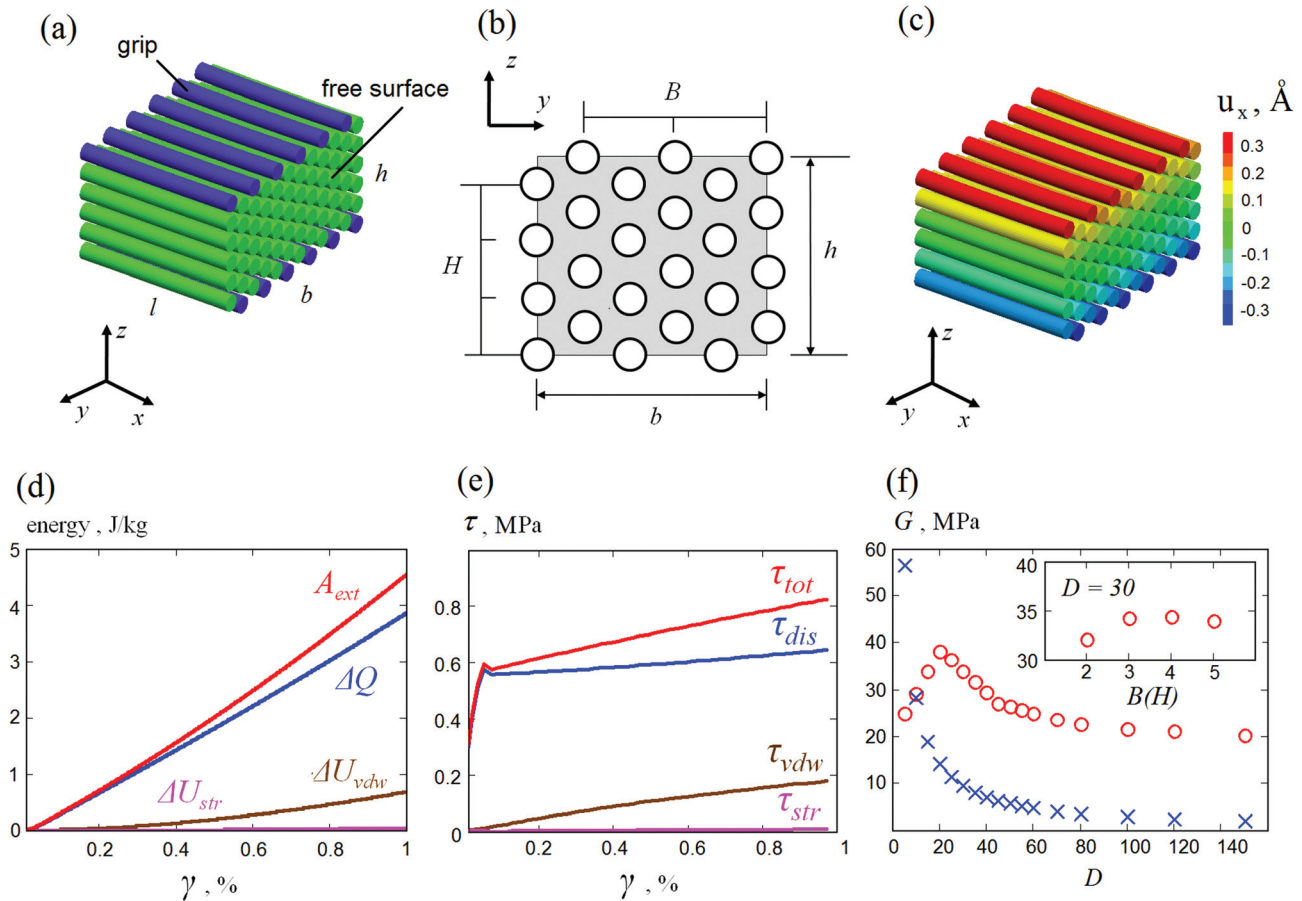


Fig. 7 Shear test on a close-packed CNT assembly. (a) Problem geometry and boundary conditions. (b) Definition of the cross-sectional area of a specimen for given values of B and H . (c) Displacement field (x component of displacement) observed in a simple shear test. (d) External work as compared to potential energy terms and dissipation during the test. (e) Decomposition of stress into vdW adhesive, elastic, and dissipative terms. (f) The influence of specimen length on its shear modulus. Red circles are simulation results, and blue crosses are theoretical predictions for the shear modulus due to surface tension. On the inset—the effect of cross section size (B and H) on the shear modulus.

presented in Fig. 6(c). They appear in certain longitudinal positions, equally spaced with period L_{CNT} in the reference configuration. After the critical strain of 40%, the specimen starts developing necks. Necking is characterized by the process of filling the vacancies developed in slip localization zones of a CNT crystal by local rearrangement of CNTs leading to formation of thinner close-packed regions (necks). Initiation of this process is accompanied by bending deformation of tubes, which leads to a jump in the strain energy (Fig. 6(a)). Necking is also characterized by a drop in (absolute) vdW adhesion energy and a slight increase in the rate of energy dissipation (Fig. 6(a)). The decomposition (Eq. (13)) for the SSC is presented in Fig. 6(b). It appears that the elastic strain does not play any significant role in the energy balance of the breaking CNT bundle. The response is dominated by dissipative forces and vdW adhesion forces (Fig. 6(b)).

3.5 Shear Test on Crystalline Assembly of CNTs. As has been demonstrated in previous sections, large CNT bundles behave as a material with the mechanical properties defined by stiffness of individual CNTs, strength of vdW adhesion between CNTs, and rate of energy dissipation during CNT sliding. However, the properties of this clearly anisotropic material with complex constitutive behavior have been studied for only one particular case of uniaxial tension. In this section, we extend our discussion with consideration of another practically relevant case of a simple shear loading of a hexagonal CNT arrangement with shear load directed along the axes of CNTs.

Consider a close-packed crystal of aligned CNTs, subjected to a simple shear test (Fig. 7). The specimen consists of hexagonally arranged CNTs with distance r_0 between CNT axes, filling a cuboid of length l , height h , and width b (Figs. 7(a) and 7(b)). The geometry of a specimen is defined by three integer parameters: number of CNTs along the width B , number of CNTs along the height H (these parameters are illustrated with Fig. 7(b)), and CNT aspect ratio D . Sizes of a specimen and number of CNTs in a cuboid are given by

$$h = r_0(H - 0.5), \quad b = \sqrt{3}r_0(B - 0.5), \quad l = TD, \quad N_{\text{CNT}} = 2BH \quad (15)$$

Periodic boundary conditions are applied along the y direction. Two surfaces of the specimen parallel to the yz plane are traction free. CNTs of two sides parallel to the xy plane are designated as grips (Fig. 7(a)). These grips are moving in a displacement control mode in opposite directions along the x axis. The gradual acceleration on the first stage of the loading is followed by motion with fixed velocity, providing a constant rate simple shear loading of a crystal.

Consider the test on a specimen with $B = 3, H = 3$, and $D = 10$. The specimen is subjected to a shear strain $\gamma_{zx} = 1\%$ at the strain rate of $\dot{\gamma}_{zx} = 2 \times 10^7 \text{ s}^{-1}$. Nominal shear strain is defined as $\gamma_{zx} = 2u_x^g/h$, where u_x^g is the grip displacement. The shear stress is defined as $\tau_{zx} = F_x/bl$, F_x is the force acting on the grip. The

Table 4 Young's modulus E , uniaxial tensile strength σ_{uts} , and critical strain ε_c , measured in experiment [9], as compared with the results of our DEM simulations

	E , GPa	σ_{uts} , GPa	ε_c , %
Experiment [9]	100–150	0.9–1.2	2–3
Simulation	70–150	0.7–1.3	1–2

indexes of stress, strain (strain rate), and shear modulus are omitted below. Figure 7(c) gives x component of displacement during the test, indicating uniform shear deformation.

Similarly to the case of simple tension, one can establish the decomposition of the SSC of the specimen into vdW, elastic, and dissipative terms. Figure 7(d) gives the energy balance during the test; Fig. 7(e) gives the stress-strain curve and its decomposition. It appears that elastic deformations of CNTs are nearly absent, and almost all work of external force is dissipated, with small fraction stored in vdW adhesion energy. Quadratic variation of vdW energy during the test dictates linear elastic response of the specimen, with a shear modulus of $G = 29$ MPa.

The shear modulus of a cuboid specimen arising from the surface tension forces can be easily estimated analytically. It follows that $G = 2\xi/l$, where ξ is the vdW surface energy per unit area of an edge surface. The surface energy $\xi = 2.6$ eV/nm² is estimated from the simulation via splitting the specimen with formation of new vdW surface. The obtained value of surface energy yields $G = 31$ MPa.

A size convergence study of material response (Fig. 7(f)) demonstrates that the specimens demonstrate size dependence of the response that is clearly conditioned by surface tension forces. A representative response is achieved for $B = 3, H = 3$, and $D = 100$. The shear modulus of representatively large specimens $G = 18$ MPa is likely conditioned by imperfect translational symmetry of vdW potential of parallel CNTs.

It is interesting to note that the crystals loaded in a direction perpendicular to CNT axes demonstrate linear elastic size-independent response with very high shear moduli of about 40 GPa, which is fully determined by the changes in vdW energy. This high shear modulus is conditioned by the interlock of CNTs in a hexagonal arrangement.

Very low values of shear modulus of CNT crystalline bundles (0.01–0.1 GPa) qualitatively agree with recent MD studies [37]. However, vdW registry features, as well as significant artificial corrugation are absent in our DEM model. Therefore, we can expect that our model underestimates shear modulus and shear strength of a CNT crystalline arrangement. In order to mimic shear behavior of CNT crystals more precisely, one needs to incorporate fine features (vdW registry corrugation) into the mesoscopic vdW potential.

4 Discussion

The results presented in Sec. 3 demonstrate that in presence of significant dissipation during CNT sliding, crystalline CNT bundles exhibit nearly uniform deformation with the material mechanical response and representative SSCs. On the other hand, without sufficient dissipation these structures develop localized slip zone at the initial stage of the deformation.

It is known that dense aligned CNT structures subjected to tensile tests in experiments [8,9] demonstrate the material mechanical response, with wide zone of plastic deformation, which is presumably associated with CNT slippage [8]. The SSCs, observed in tensile tests on fine CNT strands [9], are in good agreement with the representative SSCs obtained in our simulations. The comparison between the experiment and simulation in terms of critical strain, tensile strength, and Young's modulus are presented in Table 4.

Table 5 Total CNT-CNT force and its decomposition into contributions from the formation of a new vdW surface, dissipation and other effects, according to experimental-numerical study [31] and our DEM simulations

	Total force	vdW surface	Dissipation	Other effects
Experiment [31], nN	1.7 ± 1.0	<0.4	>0.85	<0.34
Simulation, nN	1.4	0.35	0.94	0.11

Therefore, one can suggest that forces of dissipative nature are responsible for material behavior in real aligned CNT structures [8,9]. This suggestion is supported by the results, presented in Ref. [31], where the magnitude and structure of the force acting at CNT-CNT interface in a pullout experiment were studied. It was concluded that this force is mostly conditioned by dissipation and formation of new vdW surfaces whereas other effects, such as vdW registry, were found insignificant. The decomposition (Eq. (13)) of the stress response observed in our RVE tensile test (Fig. 4(b)), renormalized in terms of an averaged force acting at each CNT-CNT contact², is very close to the one presented in Ref. [31] (see Table 5). Therefore, the parameters of SSCs observed in tensile tests (Table 4), as well as the structure of the intertube forces (Table 5) demonstrate the importance of dissipation and justify the chosen calibration of viscous damping.

Clearly, relatively high stiffness of CNTs and weak vdW adhesion determines a small amount of elastic energy that can be stored in the system, which leads to the mechanical response dominated by dissipation. The more compliant bundle systems, such as collagen fibrils, with stronger adhesion (including not only vdW interaction but also hydrogen bonds) naturally store much larger amount of elastic energy "locked" by relatively strong adhesion. This leads to a negligible role of dissipation in the mechanical response, which allows effective mechanical modeling of such systems with simple energy-conserving bead-spring models [36].

Our results were obtained for a relatively simple model of a crystalline bundle consisting of close-packed CNTs with fixed length. The more realistic models with disordered CNTs, vacancies in the crystalline structure, and random length of CNTs are expected to bring some new features, such as (i) statistical effects on stiffness, strength and ductility; (ii) initial densification and alignment of a bundle, with corresponding convex region of an SSC, similar to one observed in experiments [9]; (iii) larger size of an RVE for bundles with complex hierarchical morphologies; (iv) more complex structure of elastic energy, including bending, twisting, and shear terms; and (v) localization processes facilitated by variation in CNT length.

The presence of dissipative forces increases the strength of weakly bonded CNT structures by improving the load transfer between CNT interfaces. The bead and spring model that is widely used in mesoscopic modeling of CNT materials [19–24] provides the load transfer between CNTs due to artificial corrugation of vdW potential [30]. This property of the model leads to artifacts both in energy balance and kinematics of CNTs. In particular, it prohibits CNT sliding, rearrangements, and self-assembly processes in CNT materials. CNT models based on potentials, allowing relative CNT sliding [25,30], are able to model self-assembly processes but cannot provide sufficient load transfer between CNTs, and therefore, they are not suitable for modeling the mechanical properties of CNT materials. Our mesoscopic model, based on anisotropic vdW potential and dissipative mechanisms of load transfer between CNTs proves to be efficient in modeling both self-assembly processes (this topic was explored

²It was assumed that an average CNT in a bundle has three slipped nearest neighbors. Critical strain ε_c is used to calculate stress and its terms in Eq. (13).

in our previous work [30]) and representative mechanics of CNT structures.

5 Concluding Remarks

In this work, we applied the DEM model for CNT assemblies to study the mechanical properties of arranged close-packed CNT bundles. The key problem of energy dissipation during sliding was addressed with simple viscous contact forces, acting in parallel with vdW forces between neighboring CNTs in a bundle. In spite of this simplified approach, the model provides a quantitatively correct description of the mechanical behavior of aligned CNT structures. It was shown that sufficiently long and thick bundles behave as RVEs. It was also demonstrated that the energy dissipation during relative CNT sliding plays a central role in the material response of CNT structures. Our simplified model of energy dissipation can be improved with microscopic calibrations of rate-dependent properties, as well as intratube energy dissipation [28], in order to enable dynamic simulations of acoustic vibrations and wave propagation in CNT structures.

The DEM model applied here to model bundles of CNTs can be generalized to model other classes of nanostructures with similar properties, such as bundles of nanowires (nanobelts) and organic fibers and fibrous biological tissues [36,38,39]. The DEM model presented here is able to describe in a “hands-off” manner the extensive plastic change in response to small stress caused by the sliding of individual CNTs across each other. This early yielding behavior is highly undesirable for applications. In this respect, our current model provides a robust starting point for further investigations of various strategies aimed at enhancing the load transfer between CNTs and, thus, at improving the global strength.

Acknowledgment

The authors acknowledge financial support from Itasca Consulting Group, the National Science Foundation (Grants CMMI 0800896 and CMMI 1000415), the James L. Record Chair, and the University of Minnesota Doctoral Dissertation Fellowship.

References

- [1] Thostenson, E., Li, C., and Chou, T.-W., 2005, “Nanocomposites in Context,” *Compos. Sci. Technol.*, **65**(3-4), pp. 491–516.
- [2] Tahhan, M., Truong, V.-T., Spinks, G. M., and Wallace, G. G., 2003, “Carbon Nanotube and Polyaniline Composite Actuators,” *Smart Mater. Struct.*, **12**(4), pp. 626–632.
- [3] Hobbie, E. K., Simien, D. O., Fagan, J. A., Huh, J. Y., Chung, J. Y., Hudson, S. D., and Obrzut, J., 2010, “Wrinkling and Strain Softening in Single-Wall Carbon Nanotube Membranes,” *Phys. Rev. Lett.*, **104**(12), p. 125505.
- [4] Suhr, J., Kotakar, N., Koblinski, P., and Ajayan, P., 2005, “Viscoelasticity in Carbon Nanotube Composites,” *Nature Mater.*, **4**, pp. 134–137.
- [5] Xu, M., Futaba, D. N., Yamada, T., Yumura, M., and Hata, K., 2010, “Carbon Nanotubes With Temperature-Invariant Viscoelasticity From -196°C to 1000°C ,” *Science*, **330**(6009), pp. 1364–1368.
- [6] Thess, A., Lee, R., Nikolaev, P., Dai, H., Petit, P., Robert, J., Xu, C., Lee, Y. H., Kim, S. G., Rinzler, A. G., Colbert, D. T., Scuseria, G., Tomanek, D., Fischer, J. E., and Smalley, R. E., 1996, “Crystalline Ropes of Metallic Carbon Nanotubes,” *Science*, **273**(5274), pp. 483–487.
- [7] Yu, M.-F., Files, B. S., Arepalli, S., and Ruoff, R. S., 2000, “Tensile Loading of Ropes of Single Wall Carbon Nanotubes and Their Mechanical Properties,” *Phys. Rev. Lett.*, **84**(24), pp. 5552–5555.
- [8] Vigolo, B., Penicaud, A., Coulon, C., Sauder, C., Pailler, R., Journet, C., Bernier, P., and Poulin, P., 2000, “Macroscopic Fibers and Ribbons of Oriented Carbon Nanotubes,” *Science*, **290**(5495), pp. 1331–1334.
- [9] Zhu, H. W., Xu, C. L., Wu, D. H., Wei, B. Q., Vajtai, R., and Ajayan, P. M., 2002, “Direct Synthesis of Long Single-Walled Carbon Nanotube Strands,” *Science*, **296**(5569), pp. 884–886.
- [10] Foroughi, J., Spinks, G. M., Wallace, G. G., Oh, J., Kozlov, M. E., Fang, S., Mirfakhrai, T., Madden, J. D. W., Shin, M. K., Kim, S. J., and Baughman, R. H., 2011, “Torsional Carbon Nanotube Artificial Muscles,” *Science*, **334**(6055), pp. 494–497.
- [11] Beese, A. M., Sarkar, S., Nair, A., Naraghi, M., An, Z., Moravsky, A., Loutfy, R. O., Buehler, M. J., Nguyen, S. T., and Espinosa, H. D., 2013, “Bio-Inspired Carbon Nanotube Polymer Composite Yarns With Hydrogen Bond-Mediated Lateral Interactions,” *ACS Nano*, **7**(4), pp. 3434–3446.
- [12] Dalton, A. B., Collins, S., Munoz, E., Razal, J. M., Ebron, V. H., Ferraris, J. P., Coleman, J. N., Kim, B. G., and Baughman, R. H., 2003, “Super-Tough Carbon-Nanotube Fibers,” *Nature*, **423**(6941), pp. 703.
- [13] Behabtu, N., Young, C. C., Tsentlovich, D. E., Kleinerman, O., Wang, X., Ma, A. W. K., Bengio, E. A., Waarbeek, R. F., Jong, J. J., Hoogerwerf, R. E., Fairchild, S. B., Ferguson, J. B., Maruyama, B., Kono, J., Talmon, Y., Cohen, Y., Otto, M. J., and Pasquali, M., 2013, “Strong, Light, Multifunctional Fibers of Carbon Nanotubes With Ultrahigh Conductivity,” *Science*, **339**(6116), pp. 182–186.
- [14] Dumitrică, T., Hua, M., and Yakobson, B., 2006, “Symmetry-, Time-, and Temperature-Dependent Strength of Carbon Nanotubes,” *Proc. Natl. Acad. Sci. U.S.A.*, **103**(16), pp. 6105–6109.
- [15] Zhang, D.-B., and Dumitrică, T., 2008, “Elasticity of Ideal Single-Walled Carbon Nanotubes Via Symmetry-Adapted Tight-Binding Objective Modeling,” *Appl. Phys. Lett.*, **93**, p. 031919.
- [16] Zhang, D.-B., James, R., and Dumitrică, T., 2009, “Electromechanical Characterization of Carbon Nanotubes in Torsion Via Symmetry Adapted Tight-Binding Objective Molecular Dynamics,” *Phys. Rev. B*, **80**(11), p. 115418.
- [17] Nikiforov, I., Zhang, D.-B., James, R., and Dumitrică, T., 2010, “Wavelike Rippling in Multiwalled Carbon Nanotubes Under Pure Bending,” *Appl. Phys. Lett.*, **96**(12), p. 123107.
- [18] Berhan, L., Yi, Y. B., Sastrya, A. M., Munoz, E., Selvidge, M., and Baughman, R., 2004, “Mechanical Properties of Nanotube Sheets: Alterations in Joint Morphology and Achievable Moduli in Manufacturable Materials,” *J. Appl. Phys.*, **95**(8), pp. 4335–4345.
- [19] Buehler, M. J., 2006, “Mesoscale Modeling of Mechanics of Carbon Nanotubes: Self-Assembly, Self-Folding, and Fracture,” *J. Mater. Res.*, **21**(11), pp. 2855–2869.
- [20] Cranford, S. W., and Buehler, M. J., 2010, “In Silico Assembly and Nanomechanical Characterization of Carbon Nanotube Bucky paper,” *Nanotechnology*, **21**(26), p. 265706.
- [21] Hahm, M. G., Wang, H., Jung, H., Hong, S., Lee, S. G., Kim, S. R., Upmanyu, M., and Jung Y. J., 2012, “Bundling Dynamics Regulates the Active Mechanics and Transport in Carbon Nanotube Networks and Their Nanocomposites,” *Nanoscale*, **4**(11), pp. 3584–3590.
- [22] Xie, B., Liu, Y., Ding, Y., Zheng, Q., and Xu, Z., 2011, “Mechanics of Carbon Nanotube Networks: Microstructural Evolution and Optimal Design,” *Soft Matter*, **7**(21), pp. 10039–10047.
- [23] Li, Y., and Kroger, M., 2012, “A Theoretical Evaluation of the Effects of Carbon Nanotube Entanglement and Bundling on the Structural and Mechanical Properties of Bucky paper,” *Carbon*, **50**(5), pp. 1793–1806.
- [24] Li, Y., and Kroger, M., 2012, “Viscoelasticity of Carbon Nanotube Bucky paper: Zipping–Unzipping Mechanism and Entanglement Effects,” *Soft Matter*, **8**(30), pp. 7822–7830.
- [25] Zhigilei, L. V., Wei, C., and Srivastava, D., 2005, “Mesoscopic Model for Dynamic Simulations of Carbon Nanotubes,” *Phys. Rev. B*, **71**(16), p. 165417.
- [26] Volkov, A. N., and Zhigilei, L. V., 2010, “Mesoscopic Interaction Potential of Carbon Nanotubes of Arbitrary Length and Orientation,” *J. Phys. Chem. C*, **114**(12), pp. 5513–5531.
- [27] Volkov, A. N., and Zhigilei, L. V., 2010, “Structural Stability of Carbon Nanotube Films: The Role of Bending Buckling,” *ACS Nano*, **4**(10), pp. 6187–6195.
- [28] Jacobs, W. M., Nicholson, D. A., Zemer, H., Volkov, A. N., and Zhigilei, L. V., 2012, “Acoustic Energy Dissipation and Thermalization in Carbon Nanotubes: Atomistic Modeling and Mesoscopic Description,” *Phys. Rev. B*, **86**(16), p. 165414.
- [29] Anderson, T., Akatyeva, E., Nikiforov, I., Potyondy, D., Ballarini, R., and Dumitrică, T., 2010, “Toward Distinct Element Method Simulations of Carbon Nanotube Systems,” *ASME J. Nanotechnol. Eng. Med.*, **1**(4), p. 041009.
- [30] Ostanin, I., Ballarini, R., Potyondy, D., and Dumitrică, T., 2013, “A Distinct Element Method for Large Scale Simulations of Carbon Nanotube Assemblies,” *J. Mech. Phys. Solids*, **61**(3), pp. 762–782.
- [31] Filleter, T., Yockel, S., Naraghi, M., Paci, J. T., Compton, O. C., Mayes, M. L., Nguyen, S.-B. T., Schatz, G. C., and Espinosa, H. D., 2012, “Experimental-Computational Study of Shear Interactions Within Double-Walled Carbon Nanotube Bundles,” *Nano Lett.*, **12**(2), pp. 732–742.
- [32] Zhang, Q., Lu, Y. C., Du, F., Dai, L., Baur, J., and Foster, D. C., 2010, “Viscoelastic Creep of Vertically Aligned Carbon Nanotubes,” *J. Phys. D: Appl. Phys.*, **43**(31), p. 315401.
- [33] Carlson, A., and Dumitrică, T., 2007, “Extended Tight-Binding Potential for Modeling Intertube Interactions in Carbon Nanotubes,” *Nanotechnology*, **18**(6), p. 065706.
- [34] Johnson, S. M., Williams, J. R., and Cook, B. K., 2007, “Quaternion-Based Rigid Body Rotation Integration Algorithms for Use in Particle Methods,” *Int. J. Numer. Meth. Eng.*, **74**(8), pp. 1303–1313.
- [35] Itasca Consulting Group Inc., 2008, “PFC3D (Particle Flow Code in 3 Dimensions)” Version 4.0, Itasca Consulting Group Inc., Minneapolis, MN.
- [36] Tang, Y., Ballarini, R., Buehler, M. J., and Eppell, S. J., 2010, “Deformation Micromechanisms of Collagen Fibrils Under Uniaxial Tension,” *J. R. Soc. Interface*, **7**(46), pp. 839–850.
- [37] Li, C., Liu, Y., Yao, X., Ito, M., Noguchi, T., and Zheng, Q., 2010, “Interfacial Shear Strengths Between Carbon Nanotubes,” *Nanotechnology*, **21**(11), p. 115704.
- [38] Moore, D. F., Ding, Y., and Wang, Z. L., 2004, “Crystal Orientation-Ordered ZnS Nanowire Bundles,” *J. Am. Chem. Soc.*, **126**(44), pp. 14372–14373.
- [39] Ma, J., Liu, X., Cao, X., Feng, S., and Fleet, E. M., 2006, “Bundle of Nanobelts Up to 4 cm in Length: One-Step Synthesis and Preparation of Titanium Trisulfide (TiS₃) Nanomaterials,” *Eur. J. Inorganic Chem.*, **2006**(3), pp. 519–522.